Mass flows, turbidity currents and other hydrodynamic consequences of small and moderate earthquakes in the Sea of Marmara

Pierre Henry[1], M Sinan Özeren[2], Nurettin Yakupoğlu[3], Ziyadin Çakir[3], Emmanuel de Saint-Léger[4], Olivier Desprez de Gésincourt[4], Anders Tengberg[5], Cristele Chevalier[6], Christos Papoutsellis[1], Nazmi Postacıoğlu[7], Uğur Dogan[8], Hayrullah Karabulut[9], Gülsen Uçarkuş[3], M Namık Çağatay[3]

[1]Aix Marseille Univ, CNRS, IRD, INRAE, Coll France, CEREGE, Aix-en-Provence, France, [2]Istanbul Technical University, Eurasia Institute of Earth Sciences, Maslak, Istanbul, Turkey, [3]Istanbul Technical University, Geological Engineering Dept., Maslak, Istanbul, Turkey, [4]CNRS, DT INSU, Parc national d'instrumentation océanographique, Plouzané, France, [5]Aanderaa Data Instruments AS, Bergen, Norway, [6]Aix Marseille Univ, CNRS, IRD, MIO, Aix-en-Provence, France, [7]Istanbul Technical University, Physics Dept., Maslak, Istanbul, Turkey, [8]Yıldız Technical University, Geomatic Engineering Dept., Istanbul, Turkey, [9]Bogazici University, KOERI, Istanbul, Turkey

Correspondence to: Pierre Henry (henry@cerege.fr)

Abstract. Earthquake-induced submarine slope destabilization is known to cause mass wasting and turbidity currents, but the hydrodynamic processes associated with these events remain poorly understood. Instrumental records are rare and this notably limits our ability to interpret marine paleoseismological sedimentary records. An instrumented frame comprising a pressure recorder and a Doppler recording current meter deployed at the seafloor in the Sea of Marmara Central Basin recorded the consequences of a $M_W = 5.8$ earthquake occurring Sept 26, 2019 and of a $M_w = 4.7$ foreshock two days before. The smaller event caused sediment resuspension and weak current (< 4 cm/s) in the water column. The larger event triggered a complex response involving a debris flow and turbidity currents with variable velocities and orientations, which may result from multiple slope failures. A long delay

33   of 10 hours is observed between the earthquake and the passing of the strongest

34   turbidity current. The distance travelled by the sediment particles during the event is

35   estimated to several kilometres, which could account for a local deposit on a

36   sediment fan at the outlet of a canyon (where the instrument was located), but

37   probably not for the covering of the whole basin floor. We show that after a moderate

38   earthquake, delayed turbidity current initiation may occur, possibly by ignition of a

39   cloud of resuspended sediment.

40   ## 1. Introduction

41   Triggering of mass wasting and turbidity currents by earthquakes is a hazard

42   that can damage seafloor infrastructure (Heezen et al., 1954) and may enhance co-

43   seismic tsunami generation (Okal and Synolakis, 2001; Synolakis et al., 2002; Hebert

44   et al., 2005; Ozeren et al., 2010). Earthquake-triggered canyon flushing is also a

45   primary driver of submarine canyon development and material transfer from

46   seismically active continental margins to the deep ocean (Mountjoy et al., 2018). It is

47   often considered that a peak ground acceleration (PGA) of the order of 0.1 g is needed

48   for an earthquake to trigger a submarine slope failure (Dan et al., 2008; Nakajima and

49   Kanai, 2000). A peak ground velocity threshold of 16-25 cm/s for turbidity-current-

50   triggering has been proposed based on observations after 14 November 2016 M_w 7.8

51   Kaikoura, New Zealand, Earthquake (Howarth et al., 2021). The corresponding peak

52   ground acceleration cannot be accurately determined because the seismic waveform

53   in this study was modelled at long periods (> 2 s). Nevertheless, strong motion records

54   from this earthquake suggest this peak ground velocity threshold does correspond with

55   a peak ground acceleration of the order of 0.1 g (Bradley et al., 2017). On the other

56   hand, a global compilation of cable breaks shows that mass flows have been triggered

57   by individual earthquakes of M_w as low as 3.1 (with esdtimated PGA $\approx 10^{-3}$ g) while on

58   other margins where sediment input is relatively low and/or earthquakes frequent,

59   earthquakes >7 M_w failed to trigger cable breaking flows (Pope et al., 2016). In the

60   Mediterranean region, the threshold is reportedly around $M_w = 5$.

61   In spite of this high regional variability, turbidite deposits in several seismically

62   active zones have been used as paleoseimological event markers (e.g.: Adams, 1990;

63   Goldfinger et al., 2003, 2012; McHugh et al., 2014; Ikehara et al., 2016; Polonia et al.,

64   2016). For instance, Holocene turbidite records in the Sea of Marmara basins display

65   a recurrence of 200 to 300 years, that roughly corresponds to the recurrence interval

66 of Mw > 6.8 earthquakes (McHugh et al., 2006, 2014; Drab et al., 2012, 2015;
67 Yakupoğlu et al., 2018). Synchronicity of turbidites over a large area is considered as
68 the most robust criterion for recognizing sedimentary events caused by large
69 earthquake ruptures, although this approach has caveats (Talling, 2021; Atwater et al.,
70 2014). Distinguishing seismoturbidites, caused by earthquakes and related mass
71 wasting events, and turbidites resulting from other processes (e.g. floods, storms,
72 sediment loading) from their sedimentological characteristics is particularly challenging
73 (Talling, 2021; Heerema et al., 2022). Seismoturbidites generally comprise a basal silt-
74 sand bearing layer under a layer of apparently homogenous mud (named homogenite
75 or tail) with small or gradual, if any, variations in grain size and chemical composition
76 (Polonia et al., 2017; McHugh et al., 2011; Çağatay et al. 2012; Eriş et al., 2012;
77 Gutierrez-Pastor et al., 2013; Nakajima and Kanai, 2000; Beck et al., 2007). The grain
78 size break between turbidite and homogenite layers is however not specific to
79 seismoturbidites and can result from mud settling processes commonly occurring in
80 turbidity currents (e.g.: Talling et al., 2012). In lakes and closed basins several other
81 characteristics of turbidite-homogenites, such as the alternation of silt/sand and mud
82 laminae within a single turbidite unit and presence of bi-directional cross- or flaser-
83 bedding have been interpreted as indicators of deposition from oscillatory currents
84 associated with seiches or turbidity current reflection (Beck et al., 2007; Çağatay et al.
85 2012; McHugh et al., 2011). Indeed, internal tsunami waves and turbidity current
86 reflection have been recorded after landslides in lakes (Brizuela et al., 2019). However,
87 seismoturbidites on ocean margins have fairly similar characteristics to those in closed
88 basins but their layering has been interpreted differently, as a consequence of
89 confluence (stacked or amalgamated turbidites) or current speed variations (multi-
90 pulsed turbidites) (Gutierrez-Pastor et al., 2013; Nakajima and Kanai, 2000; Goldfinger
91 et al., 2003). There is currently a lack of in situ instrumental records that could
92 substantiate inferred hydrodynamic processes.

93 Monitoring experiments have generated observations of turbidity currents
94 flowing in submarine canyons and initiated by meteorological events, seasonal
95 discharge from rivers and occasionally by landslides (Xu et al., 2004, 2010; Puig et al.,
96 2004; Palanques et al., 2008: Liu et al., 2012; Khripounoff et al., 2012; Hughes Clarke,
97 2016; Gwyn Lintern et al., 2016; Azpiroz-Zabala et al., 2017; Paull et al., 2018; Hage
98 et al., 2019; Normandeau et al., 2020; Heerema et al., 2022). Some turbidity currents
99 originating from sediment remobilization events are driven by a thick dense basal layer,

100 able to displace and burry heavy instruments (Paull et al., 2018). On the

101

102

103 However, the hydrodynamic characteristics of turbidity currents resulting from
104 landslides and floods may not systematically differ, especially when observations are
105 done at a distance from the source (Heerema et al., 2022). Most information on
106 earthquake-triggered events is still indirect based on cable ruptures (e.g.: Gavey et al.,
107 2017; Pope et al., 2017; Hsu et al., 2008), geomorphological and sedimentological
108 observations (Mountjoy et al., 2018; Cattaneo et al., 2012; Piper et al., 1999), and
109 information from displaced instruments (Garfield et al., 1994). In Japan, in situ records
110 of pressure and temperature were obtained from displaced Ocean Bottom
111 Seismometers (OBSs) after the Tohoku 2011 M_w 9.1 earthquake (Arai et., 2013), and
112 from cabled observatories after the Tokachi-Oki 2003 M_w 8.3 earthquake (Mikada et
113 al., 2006) and after a moderate (M 5.4) earthquake off Izu Penninsula (Kasaya et al.,
114 2009). After the large events, strong bottom currents of more than 1 m/s were implied,
115 generally starting 2-3 hours after the earthquake, with no indication of oscillation or
116 pulsing. In the off-Izu case a mudflow was observed with a camera 5 minutes after the
117 earthquake and followed 15 minutes later by a change in current direction and speed.
118 We here present results from an instrumental deployment at the seafloor that
119 accidentally recorded the consequences of earthquakes that occurred 09/24/2019 and
120 09/26/2019 in the Sea of Marmara with respective M_w 4.7 and 5.8 (Figure 1A). The
121 pressure, temperature and current record from this single instrument demonstrate that
122 both events caused sediment resuspension in turbid clouds, but only the larger event
123 triggered turbidity currents. However, the instrument suffered a rather complex
124 sequence of disturbances and a 10 hour delay is observed between the earthquake
125 and peak current recording. Here, we propose a scenario which could explain the
126 observations and discuss their implications for the understanding of seismoturbidite
127 records.

128
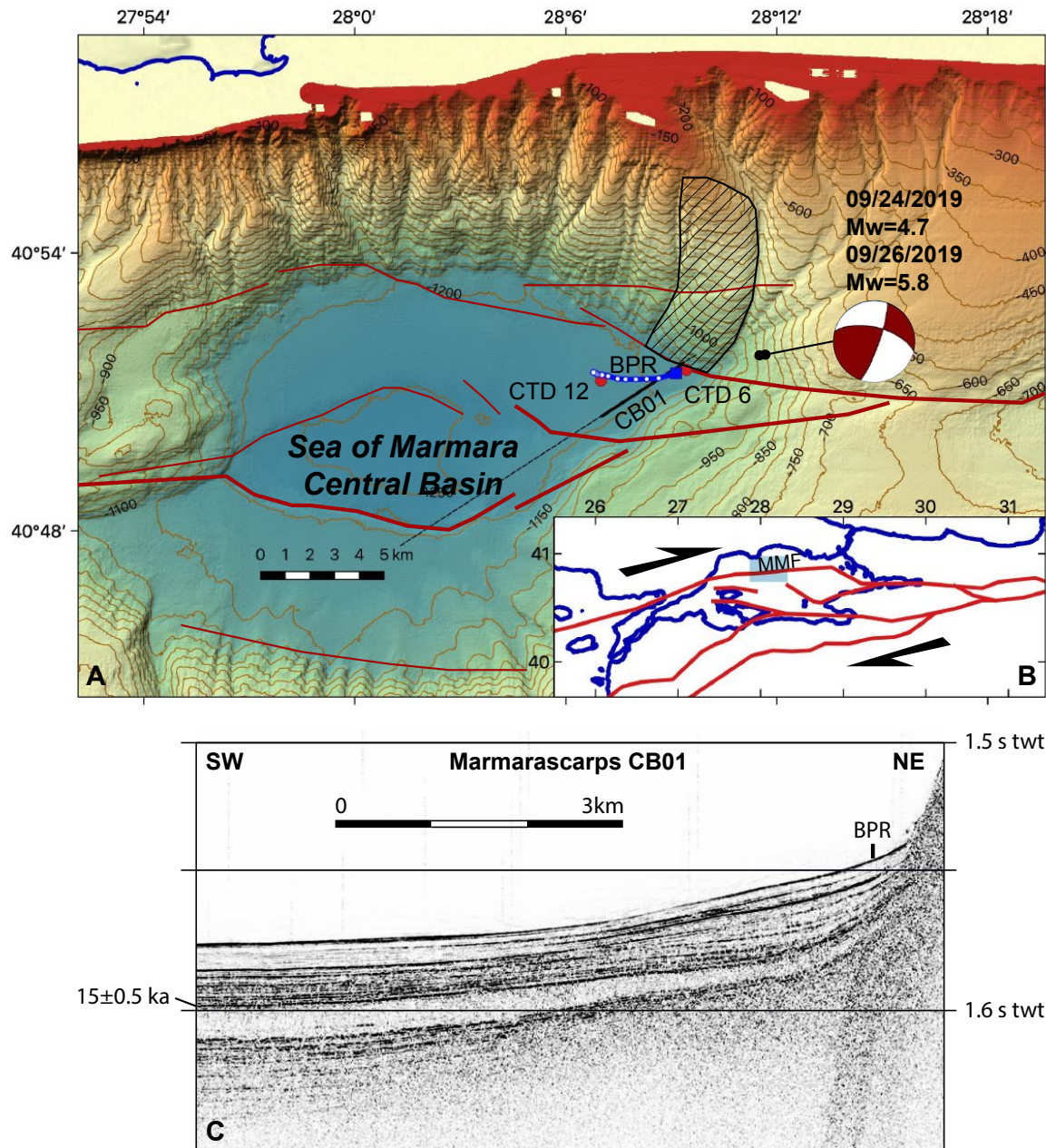
Figure 1. Context of instrumental deployment. (**A**) bathymetric map of the Sea of
Marmara Central Basin with simplified fault geometry (in red). The hatched zone is a
suspected mass wasting zone (Zitter et al., 2012). Location of instrumented frame
comprising bottom pressure recorder (BPR) and doppler current meter is indicated by
blue square. The blue banana with white dots represents the calculated trajectory of
a sedimentary particle during the waning phase of the turbidity current. Red dots are
CTD profiles 6 and 12 shown in supplementary material S1. Epicenter location of
earthquakes and the focal mechanism of the main shock are indicated. (**B**) Location
of study area. North Anatolian Fault system is shown in red. MMF is the Main

138 Marmara Fault. (**C**) Sediment sounder profile from Marmarascarps cruise (Armijo and

139 Malavieille, 2002). Indicative age of reflector from Beck et al. (2007). The instrument

140 (BPR) was deployed on a depositional fan at the base of slope and canyon outlet that

141 differ in seismic character from the reflector sequence in the basin.

2. Context and data collection

143 A series of instrumental deployments was planned to record naturally occurring

144 resonant water column oscillations (seiches) at various locations in the Sea of

145 Marmara with the aim to improve tsunami models (Henry et al., 2021). An instrumented

146 frame was thus deployed at 40.8568° N, 28.1523° E and 1184 m water depth in the

147 Central Basin on May 9, 2019 and recovered six months later (11/19/2019) (Figure 1A).

148 This site is located at the outlet of a complex canyon system with multiple confluence

149 points and tributaries originating from the edge of the continental shelf (Figure 1).

150 Sediment sounder profiles indicate a depositional fan or lobe is present at this location

151 (Figure 1C). Canyons observed on the relatively steep sedimented slope (≈10°) of the

152 Sea of Marmara deep basins are presumably fed by mass flows sourced from the

153 canyon heads and walls (Zitter et al., 2012; Çağatay et al., 2015). In addition, the slope

154 west of the canyons immediately north of the deployment site hosts a landslide

155 covering about 24 km^2 and cores taken at the base of the slope contain a sandy debris

156 flow deposit of 35-40 cm thickness buried 2 m below the seafloor (Zitter et al., 2012).

157 The Main Marmara Fault (MMF, Figure 1B), is defined as the part of the northern

158 branch of the North Anatolian Fault system crossing the Sea of Marmara (Le Pichon

159 et al., 2001, 2003). A splay of the MMF runs along the base of this slope (Armijo et al.,

160 2002; Grall et al., 2012; Sengor et al., 2014). The 09/24/2019 and 09/26/2019

161 earthquakes occurred under the canyon system and their epicenters are located 5 km

162 ENE of the instrument, less that 500 m apart (Figure 1). The rupture occurred within

163 the crust at 9-13 km depth on a northward dipping fault located north of the principal

164 displacement zone of the Main Marmara Fault. The focal mechanism indicate right-

165 lateral strike-slip with a reverse component (Karabulut et al., 2021). The rupture did

166 not reach the seafloor, nor caused a tsunami. For instance, tidal gauge records

167 obtained at Marmara Ereglisi do not deviate more than 1 hPa from a fitted tidal model.

168 The instrumentation on the frame comprises (1) an RBR bottom pressure recorder

169 (BPR) with a Paroscientific 0-2000 m Digiquartz pressure and temperature sensor, (2)

170 a Seaguard recording current meter (RCM) equipped with a Z-pulse 4520 Doppler

171   current sensor operating in the 1.9-2 MHz frequency range and other sensors:
172   temperature, pressure (tide sensor Aanderaa 5217), conductivity (Aanderaa 4319),
173   oxygen (Aanderaa optode 4330) (Figure 2). The RBR pressure and temperature
174   recording interval was set to 5s and that of the Seaguard RCM to one hour for all
175   sensors. The Seaguard instrument was fixed on the upper part of the frame and
176   sensors were 1.5 m above the seafloor. The Z-pulse Doppler current sensor is a single-
177   point current sensor, not an acoustic Doppler profiler (ADCP). It emits four narrow (2°)
178   beams paired in opposite directions along two orthogonal axes in a plane (parallel to
179   the seafloor if the frame is standing upright), and measures Doppler backscatter in
180   cells extending 0.5-to-2 m from the instrument (Figure 3). The Doppler current sensor
181   was set in burst mode, averaging 150 pings taken every second at the end of each
182   one-hour recording interval and in forward ping mode, so that only data from sensors
183   measuring a positive Doppler shift, upstream currents moving toward the instrument,
184   are used to calculate current speed. The tide sensor is a piezoresistive sensor with a
185   specified accuracy comparable to that of the Digiquartz sensors (4 kPa for a 0-2000 m
186   sensor vs. 2 kPa for a Digiquartz sensor with the same range) and 0.2 hPa (2 mm
187   ocean depth) resolution and comprises a temperature sensor of 0.2°C accuracy and
188   0.001°C resolution. The tide sensor averages pressure measured at a 2 Hz sampling
189   rate over 300 s at the end of each one-hour time interval. The tide sensor was checked
190   against an atmospheric reference between deployments and found to have a minimal
191   drift, less than 1 hPa. The main purpose of the pressure sensor records was to detect
192   long period variations in water height, related for instance to tides and seiche
193   oscillations but they are also sensitive to pressure variations caused by P-waves. In
194   addition, Digiquartz sensors are intrinsically sensitive to acceleration, but to a small
195   extent, 160 hPa/g for an instrument with 20 MPa range according to the calibration
196   report.
197   As we will show that the 09/24/2019 earthquake caused the instrumented device
198   to lay on its side for several hours and then straighten up, understanding the setup of
199   the seafloor device and its stability is important (Figure 2B). The frame is made of
200   aluminium and has six rigidly bound flotation spheres of 25 kg buoyancy each. The net
201   weight of the instrumented frame in water is -80 kg. The frame is rigidly attached to a
202   12-cm-thick 1.5x1.3 m concrete slab, weighing 300 kg in water. The assembly of the
203   heavy slab and buoyant frame is stable in an upright position in the water and on the
204   seafloor. Moreover, it is estimated that a current of 1 m/s would cause a total horizontal

205   drag of 75 kg (≈750 daN) when the device is in upright position, which is insufficient to

206   destabilize it. If a stronger current, or other external forces, cause the assembly to tilt

207   and lay on one side, the moment of the gravity and buoyancy forces should straighten

208   the device back to upright position when these external forces are removed.

209   Measurement of current speed and direction by a tilted instrument is a related issue

210   that we here consider. The orientation and attitude of the Seaguard RCM is measured

211   with a 2-component accelerometer and a magnetic compass and the recorded data

212   include tilt in X and Y direction and the heading of the X axis. Tilt X and Y components

213   are factory calibrated from -35° to +35° with an accuracy of 1.5°. Tests performed in

214   the laboratory (see supplementary material, Figure S1) showed that tilt information

215   remains consistent outside this range, even when the instrument is upside down. Tilt

216   measurements are accurate within 3° up to 60° but saturate at about 80° (Figure S2).

217   Uncertainty on heading also increases with tilt, especially when the instrument is tilted

218   toward the X-direction. However, measured heading remains ±20° of true heading for

219   a tilting of up to 60° (Figure S3). The current measured in the instrument plane is

220   corrected for tilt assuming current is horizontal. As far as this approximation is valid,

221   the current record should in principle remain fairly accurate when the instrument is

222   tilted beyond the normal range of operation (±35° degree) and at least to 60°. However,

223   the compass was not calibrated for an upside-down configuration. If the top of the

224   instrument would happen to be oriented downward, the measured current direction will

225   be unreliable, even though the absolute speed may still be correctly estimated. Another

226   problem may arise if one of the Doppler sensors is facing down into the sediment so

227   that its measurement cell is below the seafloor. If the sensor pointing upward in the

228   opposite direction is recording a negative Doppler shift, this value will be ignored in the

229   forward ping mode. In this case, the measurement retained to calculate current velocity

230   will correspond to noise from the sensor facing toward the seafloor. In all situations, it

231   remains possible to recalculate the sensor readings retained by the calculator from the

232   current velocity and orientation parameters recorded by the instrument by projecting

233   the velocity vector back in the instrument plane, and thus assess the reliability of data.

234   The strength of the backscattered signal can be used as a proxy for turbidity. The

235   Z-pulse emits in the 1.9-2 MHz band corresponding to a wavelength (λ) of 750 µm.

236   Doppler backscatter current meters have maximum sensitivity for particles of diameter

237    $D = \lambda/\pi$ and can detect particles down to diameter $D = 0.08\ \lambda$, for which backscatter

238   power is less than 1/10 of peak backscatter power (Guerrero et al., 2011, 2012). The

239 seaguard RCM should thus be mostly sensitive to the presence in suspension of larger
240 than 63 µm. This, however, does not imply that the detected particles are all sand
241 grains in the mineralogical sense, as clay flocs of the same size also cause
242 backscattering,
243

A. instrument

- Acoustic releaser
- Doppler current sensor
- Tide pressure sensor
- Seaguard data logger
- Flotation sphere
- Digiquartz pressure sensor
- Binding chain
- Aluminium frame
- Concrete ballast

B. forces

150kg
40 kg
30 kg
1.30 m
1.40 m
300kg
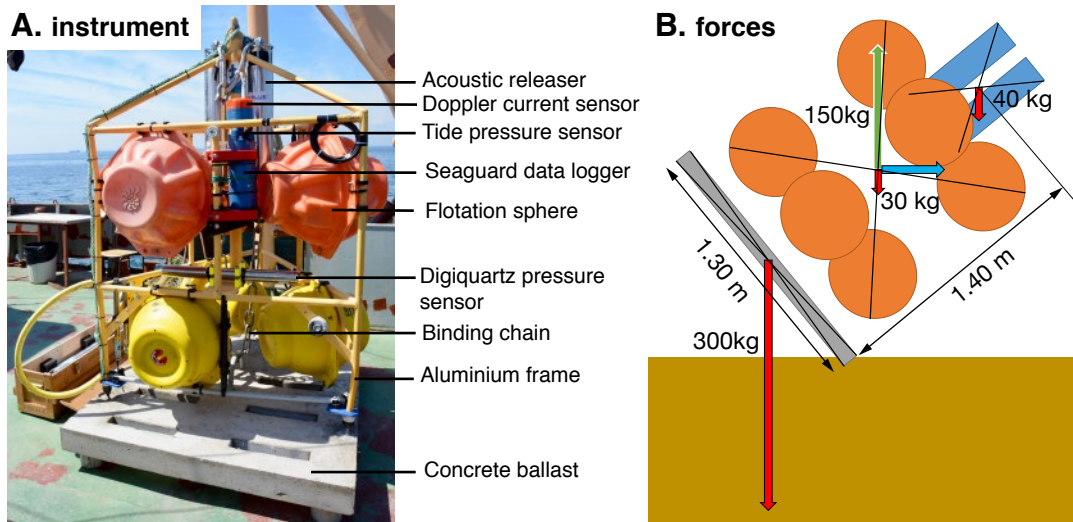
244
245 **Figure 2.** Instrumented frame. (A) photo of the instrumented frame before
246 deployment. (B) Sketch showing forces applied to the elements of the instrumented
247 frame in water. The red arrows represent the weight in water of the cement ballast, of
248 the instrumented frame and of the acoustic release system on top. The green arrow
249 represents the buoyancy of the flotation spheres. The blue arrow represents the
250 current drag, which depends on current speed and instrument tilt.
251
252
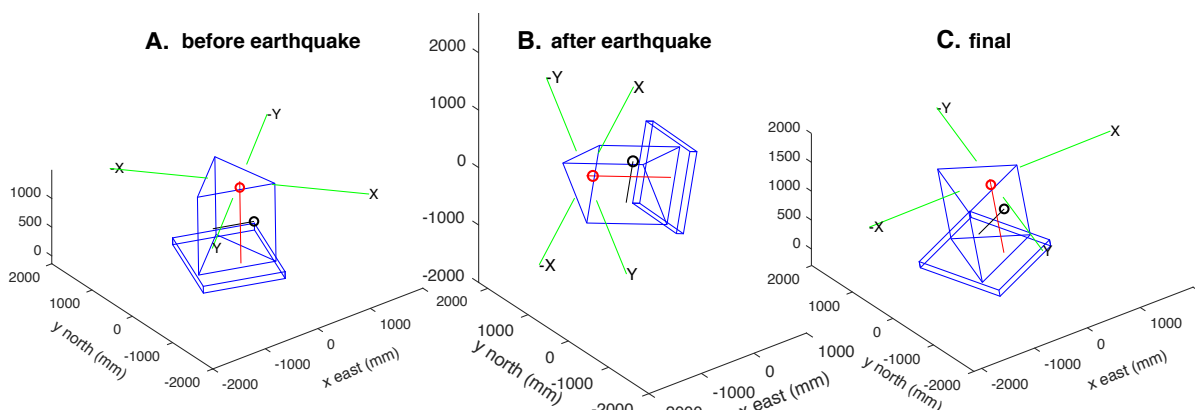
253
254 **Figure 3.** Reconstruction of frame position based on instrument tilt-meter and
255 compass data: (A) before the earthquake; (B) Tilted, between, 25 minutes and 10.5
256 hours after earthquake; (C) back in nearly upright position 11 hours after earthquake.

257 Position of Digiquartz pressure sensor (black circle), Aanderaa tide sensor (red

258 circle) and Doppler current meter beam cells (green segments)

259

260 ## 3. Results

261 ### 3.1. Pressure and tilt records

262 Small earthquakes are detected as pressure spikes, while oscillations are

263 recorded after large earthquakes. The M_w 4.7 09/24/2019 caused a short pressure

264 transient of 25 hPa at 08:00:26 followed by small pressure oscillations of less than 3

265 hPa amplitude decaying over a few minutes. The seismic wave train from the M_w 5.8,

266 09/26/1919 earthquake is recorded by the Digiquartz pressure sensor as oscillations,

267 initiated by a pressure drop of 65 hPa between 10:59:22 and 10:59:26 (Figure 4). For

268 the sampling interval of 5s used in this setup, the recorded signal is aliased, which

269 precludes quantitative interpretation in term of velocity or acceleration. However, the

270 initial pressure drop after the 09/26/1919 earthquake may indicate a negative polarity

271 of the first P-wave arrival at the instrument site, located on an ascending ray-path.

272 Twenty-five minutes after the M_w 5.8 earthquake, a new disturbance of the

273 pressure sensor is observed at 11:23:41. The pressure then progressively increases

274 by 30.9 hPa in 15 seconds between 11:24:46 and 11:25:01 before stabilizing. Over the

275 corresponding one-hour-time-interval between successive records, the Seaguard

276 RCM, initially subvertical (tilt less than 2°), acquires a strong tilt (Figure 3). At 11:57:48,

277 measured tilt is -65° along the X-axis and +19° along the Y-axis, with X-axis in a N161°

278 azimuth and these values remain constant ±2° over the next 10 hours, corresponding

279 to an absolute tilt of 68° (Figure 4). The tilting of the instrument causes the Digiquartz

280 and Tide sensors to record different pressure variations because they are located at

281 different positions on the frame (Figure 2). Moreover, the pressure readings by the

282 Digiquartz sensor also depend on its orientation relative to Earth gravity. Pressure at

283 the Tide sensor location increases about 100 kPa, corresponding to a 1 m drop and

284 indicating that the frame was then practically laying on its side. Ten hours later, the

285 device apparently straightens itself in about 5 seconds, between 21:28:29 and

286 21:28:34 as indicated by a rapid pressure variation. After that, the recorded tilt

287 parameters are moderate and stabilize at -11.5° for the X-axis and 5.3° for the Y-axis,

288 with X-axis in a N105.3° azimuth.

289   Baseline changes before and after the earthquake correspond to an increase of
290 23 hPa for the Digiquartz sensor and 20 hPa for the Tide sensor. These concur that
291 the instrumented frame was about 20 cm deeper after returning to upright position.
292 Considering that the slope at the location of the instrument is about 1%, this may
293 correspond to a 20 m lateral downslope displacement. However, in the absence of
294 other information, it is not known whether the pressure baseline change is a
295 consequence of instrument lateral displacement or burial in place.

296   The M_w 4.7 earthquake caused minor disturbances of the attitude of the
297 instrument, with variations of tilt and heading of less than 0.5°. A M_w 3.6 foreshock of
298 the M_w 5.8 occuring 26/09/2019 at 7:32 also caused minor disturbances. These
299 indicate that the seafloor was sensitive to ground shaking caused by these small
300 earthquakes. However, this did not cause the device to sink into the sediment.
301 Changes of the pressure baseline of the digiquartz sensor between before and after
302 these earthquakes are difficult to resolve, and correspond to less than 5 mm vertical
303 displacement for the first event and less than 2 mm for the second one.

304

305
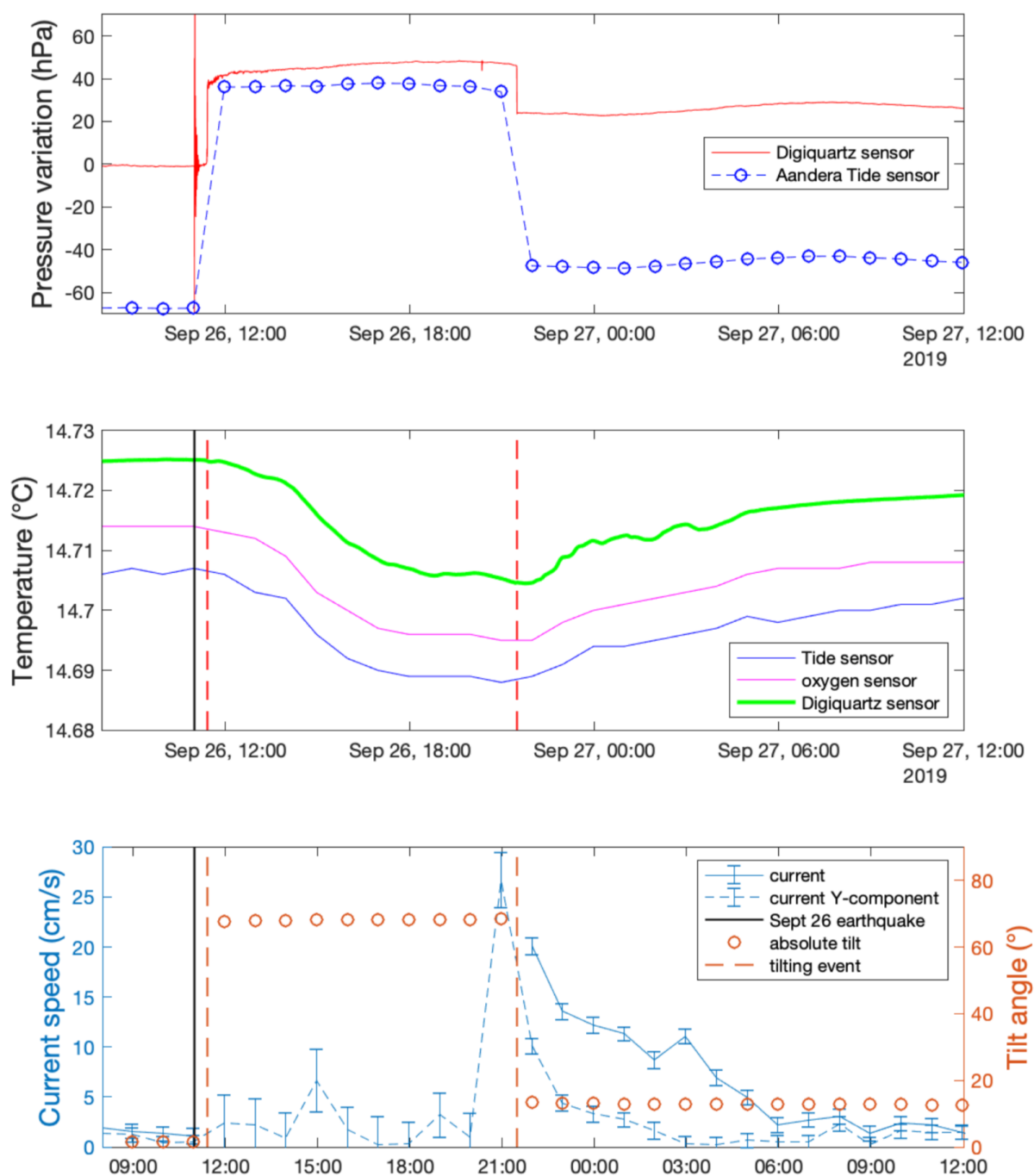
Figure 4. Time series around the time of occurrence of a M_w 5.8 earthquake; (top) pressure variations recorded by two instruments on the instrumented frame; (middle) temperature records from Digiquartz, Tide and oxygen sensors, (bottom) current and tilt data recorded by Seaguard RCM. Between the tilting events only one component of the doppler current meter functioned reliably (Y-component oriented N200) and is here reported.

313

314
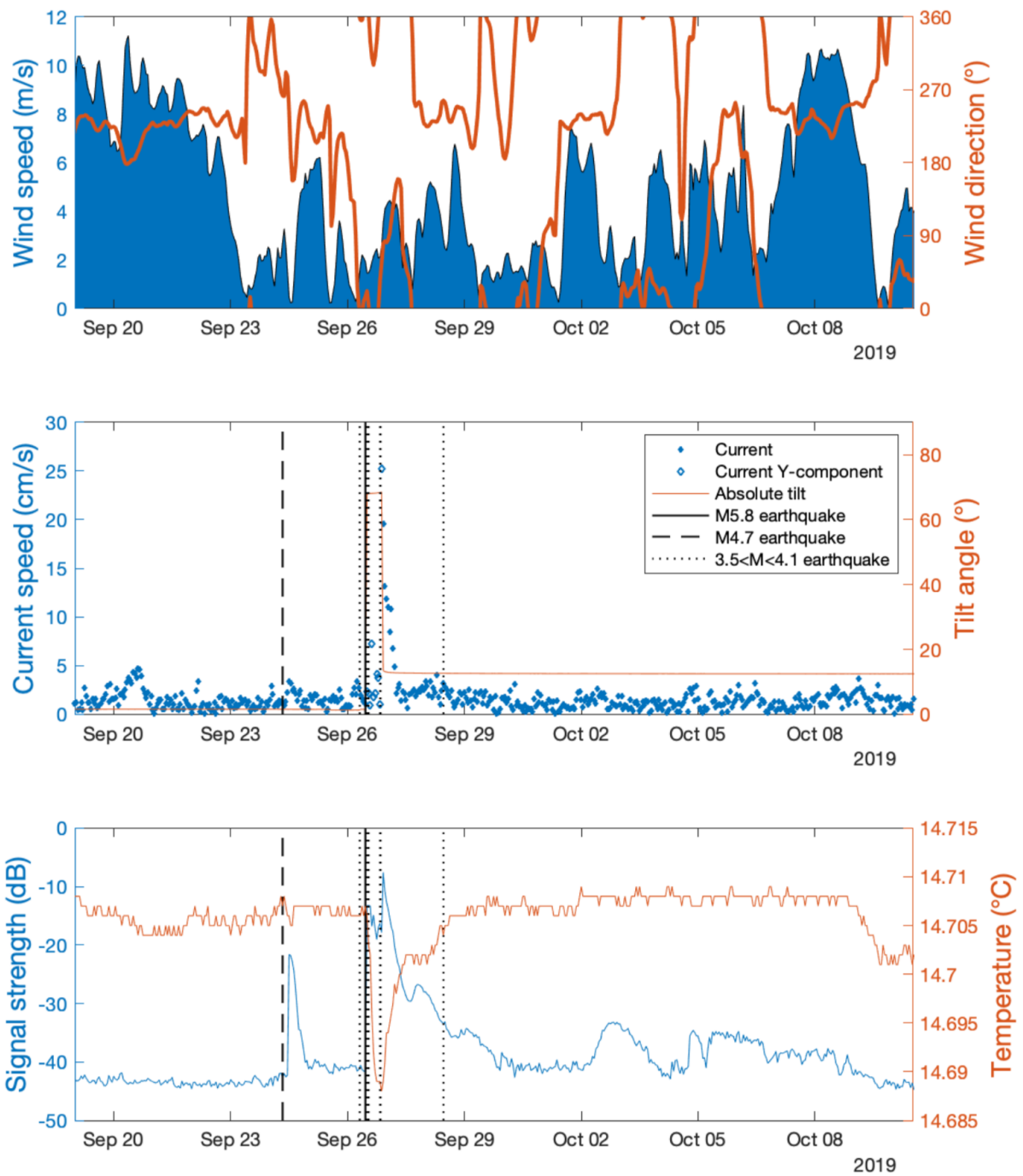
315 **Figure 5.** Time series acquired with Seaguard RCM during the September 2019

316 seismicity cluster and ERA5 reanalysed meteorological data (Hersbach et al., 2018);

317 (top) ERA5 wind data (middle) current speed and tilt; (bottom) backscatter signal

318 strength and temperature.

319

    3.2. Current records

321   The M$_w$ 4.7 09/24/2019 earthquake was followed by a small increase of current

322   strength peaking at 3.4 cm/s at noon, four hours after the earthquake (Figure 5).

323   Comparable events in term of duration and strength occurred spontaneously

324   09/20/2019 (with currents up to 4.7 cm/s) and 09/26/2019 (with currents up to 3.3 cm/s)

325   just before the M$_w$ 5.8 earthquake. During all three events the dominant current was

326   from the east, thus coming from the direction of the canyon, but there is an important

327   difference between the event that occurred after the M$_w$ 4.7 earthquake and the two

328   others. During that event a change in current direction occurred from eastward to

329   westward between 10:57 and 11:57 while the current strength increased from 2.2 cm/s

330   to its peak value of 3.4 cm/s (Figure 6). During the other events, build-up was more

331   progressive and did not involve a change in direction. A drift plot, calculated by

332   summing velocity vectors over time, reproduces the motion of a particle assuming a

333   uniform velocity field (Figure 6). The total drift occurring in the 8 hours following the

334   current inversion is about 500 m. Current direction varies from westward to northward

335   during this time interval.

336

337

338
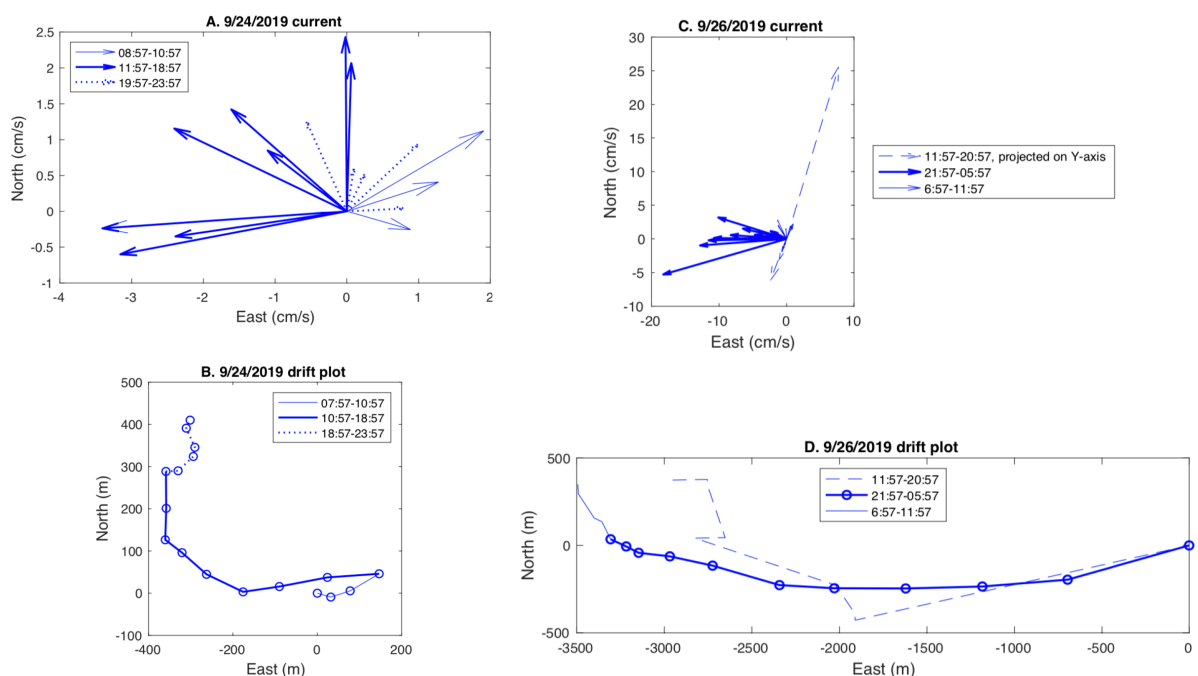
339   **Figure 6.** Current recorded after M$_w$ 4.7 and M$_w$ 5.8 earthquakes: (A) Current velocity

340   arrows recorded every hour between 08:57 and 23:57 on 09/24/2019; (B) drift plot

341   over the same time interval, the change of current direction and strength between

342 10:57 and 11:57 coincides with increasing backscatter strength (see figure 4),

343 indicative of increased turbidity; (C) Current velocity arrows recorded every hour

344 between 12:00 09/26/2019 and 06:00 09/27/2019. Dashed arrows show

345 measurements acquired in the Y direction when the instrument was strongly tilted

346 (position B in Figure 3), plain arrows when it was back in upright position (C in Figure

347 3); (D) drift plot over the same time interval, the dashed part corresponds to the

348 strongly tilted position.

349

350   After the M_w 5.8 09/26/1919 earthquake, during the 10 hour period when the

351 instrument remained strongly tilted, the instrument recorded currents varying both in

352 speed and orientation, but some precautions are needed when interpreting these data.

353 The current component measured by transducers along the Y-axis of the instrument,

354 oriented N200°, probably remained accurate as the tilt along this axis is less than 20°

355 and the measurement cell remained above the bottom (Figure 2B). On the other hand,

356 the X-component may not be reliable as one of the sensors (n°1) is oriented 65°

357 upward in the N160° direction, and the oposite sensor (n°3) is dipping 65° downward

358 in the opposite (N340°) direction. Consequently, measurement cell n°3 lies within the

359 sediment and thus may only record noise. Moreover, because the Doppler current

360 sensor (DCS) is set in forward pinging mode, current speed is calculated with data

361 from sensors measuring positive doppler shifts only. This implies that if the current

362 component toward N160° is positive, sensor n°1 will measure a negative shift and will

363 not be recorded. During the time inteval considered here, the mesured current

364 component in the X-direction (toward N160) is positive, which indicates that data from

365 sensor n°3 was used (Figure 7), and that is probably noise. It follows that the current

366 component along the Y-direction is the only one reliable. The horizontal current

367 measured along the Y-axis changed sign several times during this time interval, and

368 reached peak values of 6.3 cm/s toward N200 at 14:57:46, about four hours after the

369 earthquake, and of 25 cm/s in the opposite direction at 20:57:46, the last measurement

370 before the instrument straightenned up. Other measurements on both axes remain

371 below 5 cm/s, but the absolute velocity may have been higher because this

372 measurement was only performed in one direction. Yet, these observartions suggest

373 that the stronger current (25 cm/s) recorded 30 minutes before the instrument

374 straightenned up played a role in this event. Once the device got back in an upright

375 position, it recorded a current consistently flowing westward and progressively

376 decreasing from 20 cm/s to background level (2 cm/s) in nine hours (Figure 4). During

377 this waning phase, the current drift is about 3.5 km in a westward direction (Figure 6).

378 The drift estimated during the first 10 hours after the earthquake, while the instrument

379 was strongly tilted, is in the opposite direction but may not be reliable.

380

381
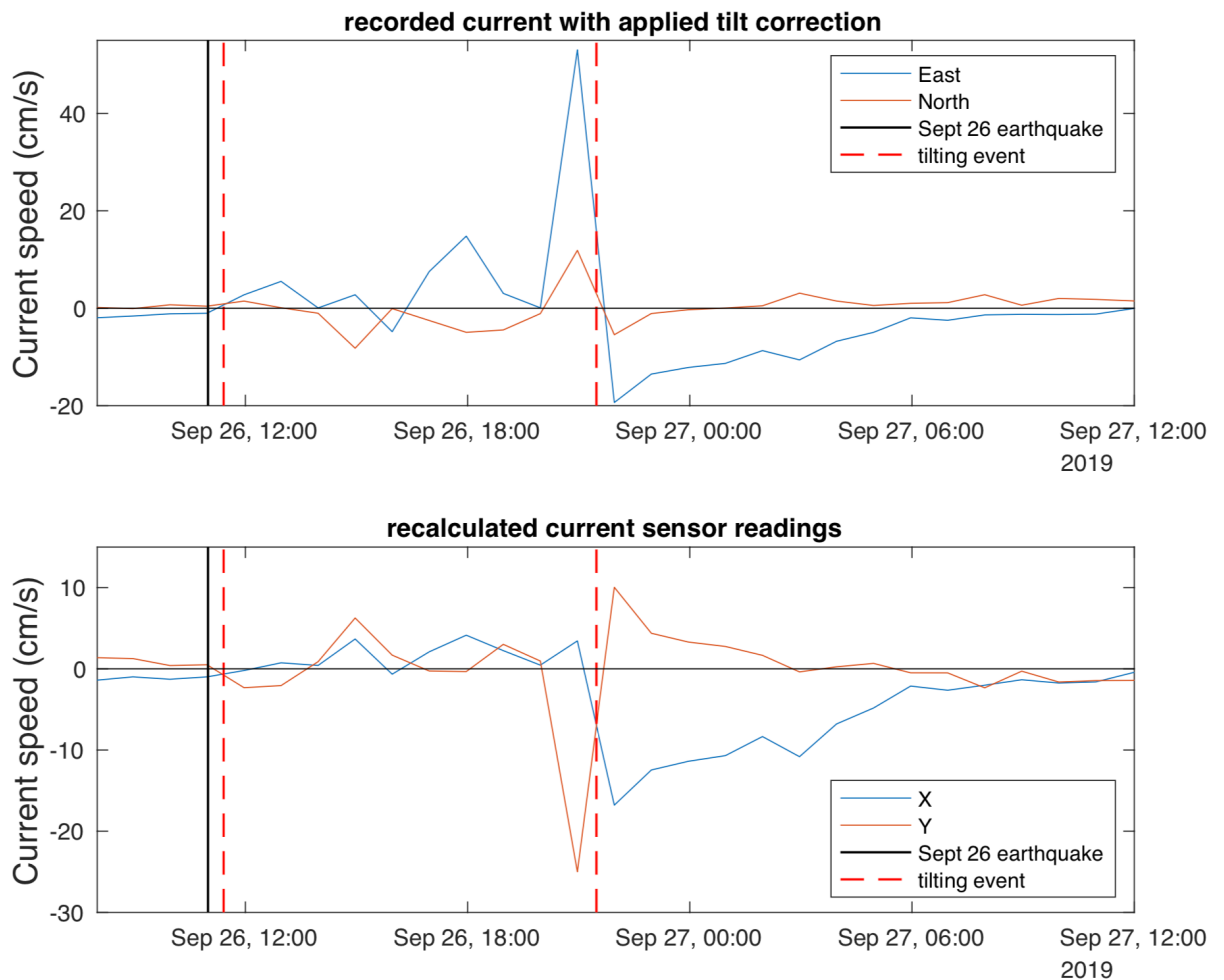
382 **Figure 7.** Current record acquired around the time of occurrence of a M_w 5.8

383 earthquake. A. Instrumental record, automatically corrected for tilt and heading. B.

384 recalculated readings in the X and Y axis of the Doppler sensor (see text for

385 interpretation).

386

387   3.3. Acoustic backscatter signal

388   The background backscatter amplitude level is -43±1dB before the earthquakes.

389 Three to four hours after the M_w 4.7 09/24/2019 earthquake, backscatter increases

390 sharply to -22dB between 11:00 and 12:00, and then decays to -41dB over 12 hours.

391 The increase of backscatter coincides with a change of current direction and speed,

392 indicating that the turbid cloud was brought to the instrument site by the current.
393 However, the current speed of less than 4 cm/s may have been insufficient to put the
394 particles in suspension. There is no increase of backscatter on Sept 20 when stronger
395 currents coming from the same direction, but not related with an earthquake, were
396 recorded.

397   Backscatter strengh remains -41±1 dB for the 1.5 day interval before the M_w 5.8
398 09/26/1919 and increases to the -20 dB to -13 dB range after the earthquake (Figure
399 5). This implies sand sized particles or flocs were put in suspension soon after the
400 earthquake although the local current speed remained relatively low (about 5 cm/s at
401 most). After the device went back to near vertical position, signal strengh reaches a
402 maximum of -7.6 dB, which correspond to an amplitude ratio of 42 and an intensity
403 ratio of 1800 compared to base level. Similar signal strength levels are typically
404 reached with the Z-Pulse sensor in highly turbid water such as in estuaries. During
405 deep sea deployments signal strength range more typically between -60 and -40 dB.
406 After reaching peak value, backscattered signal strengh progressively decays over 3
407 days to stabilise at about -40 dB (Figure 5). Several turbid events, with signal strength
408 about -35 dB are observed in October and associated with small increases in current
409 velocity (up to 3-4 cm/s). It is unclear whether these passing clouds are residual
410 turbidity from the earthquake. After October 9, backscatter eventually returns to
411 background level while temperature decreases by 0.007 °C over a few hours,
412 indicating replacement of the water mass around the instrument.

413

414   3.4. Temperature record

415   The Sea of Marmara is stratified, with a low salinity (20-22‰) 20-30 m surface
416 layer that displays strong seasonal temperature variability (5-10°C in winter, 20-25°C
417 in summer) overlaying a high salinity (about 38‰) body of seawater at 14-15°C derived
418 from the Aegean Sea (Beşiktepe et al., 1994). Within the high salinity body, the
419 conservative temperature (McDougall et al., 2013) calculated with the Gibbs Seawater
420 oceanographic toolbox of TEOS-10 (McDougall and Barker, 2011) generally
421 decreases with depth. This implies that the adiabatic temperature rise in a turbidity
422 current, flowing downward, should cause a small temperature increase at the location
423 of the instrument. However, the deployment site is prone to seasonal cascading within
424 the deep water body, so that the initial temperature structure may have been disturbed.

425   Examples of CTD profiles recorded in June 2007 (Henry et al., 2007) are shown in
426   Figure 8 and indicate the presence of a slightly warmer water body on the seafloor,
427   only present in the basin along the base of the slope. No CTD profile is available in
428   Sept 2019, but variations in temperature and oxygen concentration associated with
429   mild currents (<5 cm/s) were recorded by the instrument in May-July 2019, and again
430   on Sept 20. It is therefore likely that the temperature at the location of the instrument
431   was slightly higher, by 0.01 to 0.02°C, than at the same depth in the central part of the
432   basin.

433   Temperature variations associated with the M_w 4.7 09/24/2019 earthquakes are
434   very small, less than ±0.002°C, which confirms that water movements during this event
435   were local. After the M_w 5.8 09/26/1919 earthquake the recorded temperature
436   decreases progressively by about 0.015°C to reach its minimum value when the
437   strongest current is recorded, around the time when the instrument straightens itself
438   (Figure 5). After that, temperature progressively increases back to reach nearly the
439   same value as before the event. The small variation in temperature indicates that the
440   turbid water originates from within the deep-water body. One remarkable observation
441   is that temperature only starts decreasing very slowly after the tilting of the instrument.
442   Temperature decreases at a higher rate after 14h, which is also when the tilted
443   instrument start measuring significant currents.

444   The slight temperature decrease observed after the earthquake can result from
445   the mixing of the warmer bottom water body originally present around the instrument
446   with the bulk of the deep-water layer in the Central Basin. Moreover, the observation
447   of a temperature drop precludes that the turbid water originates from depths less than
448   600 m, as water present between 600 m and the halocline is at a higher conservative
449   temperature than the deeper water throughout the year (see Beşiktepe et al., 1994,
450   and figure 8). Moreover, an inflow of water from closer to the surface should result in
451   an increase in the O_2 concentration in the bottom water, but none is observed in the
452   data.

453
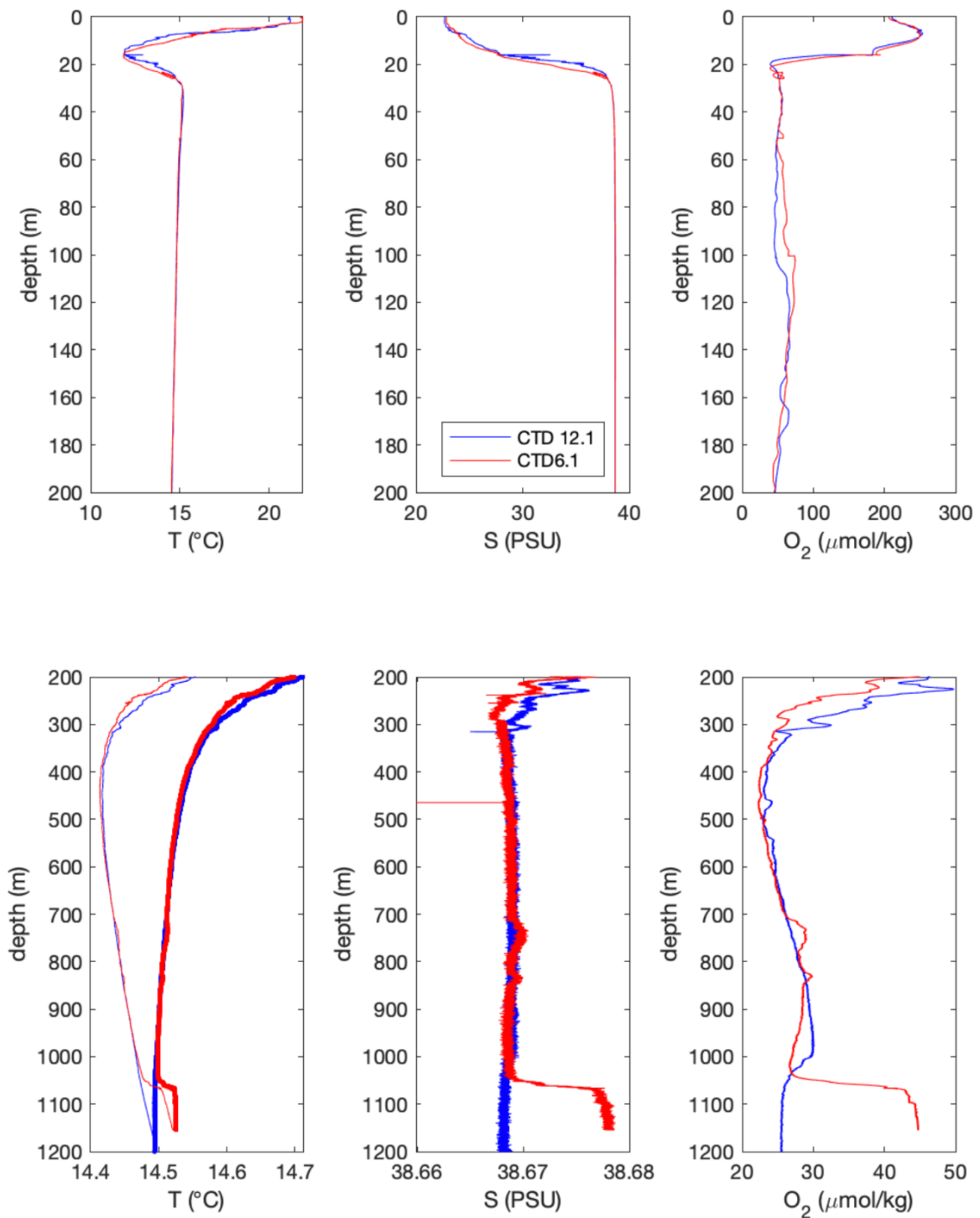
Figure 8. Depth plots of Temperature (°C), Salinity (PSU) and oxygen concentration (μmol/kg) from CTD profiles acquired in the Sea of Marmara in June 2007 during Marnaut cruise of Ifremer RV L'Atalante (Henry et al., 2007). On the lower temperature plot, thin lines are measured values and thick lines are conservative temperatures calculated at 1180 m. Locations are shown on Figure 1

4. Interpretation and discussion

4.1. Sequence of events

Let us first consider the potential influence of meteorology on the events recorded at the seafloor. Reanalysed ERA5 hourly wind and pressure data (Hersbach et al., 2018) interpolated at the location of the instrument indicate relatively low wind (less than 5 m/s) at the time of the earthquakes and during the hydrodynamic disturbances that followed (Figure 5). It is thus unlikely that wind influenced the course of these events. On the other hand, the current event on 20/09/2022 occurs at a time of high wind and follows a change of wind direction. Hypothetically, wind forcing may have caused this event, but probably not through sediment resuspension as acoustic backscatter remained low. A possible influence of wind on the motion of turbid clouds passing over the instrument after October 2 remains open for discussion.

The observations at the seafloor provide some insight on the complex sequence of events that followed the earthquakes and suggest the following scenarios. After the M_w 4.7 09/24/2019 a turbid cloud formed east of the instrument and drifted slowly. Considering the maximum velocity of the current (less than 4 cm/s) and the 4-hour interval between the earthquake and the passing of the turbid cloud over the instrument, the front of turbid water should have formed East North East of the instrument at a maximum distance of about 500 m, and this coincides with the base of the northern slope near the outlet of the canyon. Small scale failures on the steeper slopes on the sides of the canyon and shaking are possible causes of sediment resuspension. The clouds subsequently drifted downslope over a total horizontal distance of at most 1 kilometers before dissipating, adding the 500 m estimate above to the drift calculated after the passing of the front over the instrument (Figure 6).

The M_w 5.8 09/26/1919 caused stronger currents and a small temperature perturbation. Temperature records from turbidity currents invariably display a correlation between current onset and temperature change and this temperature change is nearly always positive (Mikada et al., 2006; Palanques et al., 2008; Kasaya et al., 2009; Xu et al., 2010; Khripounoff et al., 2012; Liu et al., 2012; Hughes Clarke et al., 2006; Johnson et al., 2017; Brizuela et al., 2019; Normandeau et al., 2020; Heerema et al., 2022). Temperature spikes may thus be used to infer turbidity current occurences and provenance (Johnson et al., 2017). That the currents we observe are associated with a temperature decrease rules out that they initiated at the shelf edge

494 as water above 600 m depth is at a higher potential temperature (temperature
495 corrected for the adiabatic gradient) than water at the seafloor (Figure 8). Water may
496 have been mixed locally or flowed down some distance down the slope. For instance,
497 currents may have originated from above the earthquake rupture zone, where the
498 seafloor lies in the 600-to-1200 m depth range.

499 The temperature records also concur with the current record to indicate that
500 currents in the water column remained moderate for several hours after the earhquake
501 and are not the primary cause of instrument tilting. First of all, there is a delay of at
502 least one hour after the earthquake (30 minutes after the tilting event) before
503 temperature starts decreasing significantly. Moreover, an acceleration of the
504 temperature rate of variation correlates with an increase in measured current speed
505 (to about 6 cm/s) between 14h and 15h (about 2 hours later), indicating that the tilted
506 current meter and the termperature sensors are providing concordant information.
507 Even if a short burst of current may have been missed because of the 1 hour interval
508 between current records, this would not explain why the frame remained stable in a
509 tilted position for several hours. Local liquefaction of the sediment beneath the device
510 is also an unlikely cause because the tilting of the instrument occurred 25 minutes after
511 the earthquake. A thin dense flow of remobilized sediment originating from the basin
512 slopes thus appears as a more likely cause. Partial burrial of the device is attested by
513 presence of sandy mud caked on the device in various places: on the frame feet, on
514 the acoustic releases, on the optode connector and, also inside the plastic protection
515 of a flotation sphere from which bindings were broken. On the other hand, the current
516 speed of at least 25 cm/s recorded before the time when the device straightened up is
517 strong enough to cause erosion of mud deposits. It may thus be hypothesized that
518 erosion freed the device from the mud cover. The flotation spheres on the frame and
519 the concrete ballast at its base exert a moment that should keep the assembly stable
520 in an upright position unless the frame is loaded with sediment.

521 Powerful turbidity currents driven by dense basal flows have notably been
522 observed in Monterey Canyon (Paull et al., 2018) and may share some characteristics
523 with the event reported here, although this event is much weaker. These dense flows
524 are relatively thin (< 2 m in the Monterey Canyon case) and have the ability to displace
525 instruments before the development of turbulence in the water column. It appears likely
526 that, after the passing of the seismic wave, failures on slopes adjacent to the
527 deployment site caused a debris flow or dense mud flow that spread on the basin floor

528 causing the tilting of the instrument and bottom water turbidity while turbulence in the
529 water column remained limited. As the base of the nearest slope is about 400 m north
530 of the instrument, this would imply a minimum velocity of 20 cm/s for the mudflow to
531 reach the device location in 25 minutes.

532   During the following 10 hours, the current record is incomplete but indicates
533 variations in strength and direction. One possible explanation is that widespread slope
534 instabilities triggered by the earthquake have resulted in several turbidity currents
535 recorded as succesive pulses. Other possible explanations include oscillatory currents.
536 However, the role of seiches and surface gravity waves can be ruled out as no tsunami
537 was recorded by near shore tidal gauges around the Sea of Marmara. The relationship
538 between gravity wave amplitude A and bottom current amplitude U in the shallow water
539 linear approximation is given by $U=(g/H)^{1/2}A$, where H is water column height. An
540 oscillatory current of 10 cm/s at 1200 m depth would thus correspond to a free surface
541 oscillation of 1 m (or 100 hPa) for a standing wave (seiche) as well as a progressive
542 wave (tsunami). This should have been easily detected in a sea where tidal amplitude
543 is about 10 cm (Alpar and Yüce, 1998). The influence of baroclinic internal waves on
544 the halocline at 20-30 m depth must also be ruled out as they cannot physically
545 produce currents of more than a few cm/s at 1200 m. Nevertheless, It remains possible
546 that the interface at the top of the turbid cloud is affected by baroclinic waves.

547   The strongest current is recorded after 10 hours, which suggests that a turbidity
548 current initiated further upslope (but deeper than 600 m) may have reached the site
549 after a longer delay but may also have gained more kinetic energy on its downhill path.
550 This event, reaching a speed exceeding 25 cm/s apparently caused enough erosion
551 to free the device from the mud accumulation. The current then stabilizes in a westward
552 direction and decays progressively over the next 9 hours, which suggests the tail of a
553 turbidity current flowing in the canyon E of the deployment site has been recorded. The
554 hours-long delay between the earthquake and the passing of the fastest current over
555 the instrument may hypothetically correspond to the time for the head of the turbidity
556 current to travel from its source to the location of the instrument. Alternatively, a
557 sequence of slope failures may have lasted up to several hours after the earthquake.
558 Longer delays between loading events and turbidity currents, of several days to,
559 possibly, months, have been observed after floods (Carter et al., 2012) or after distant
560 earthquakes (Johnson et al., 2017). Another possibility is delayed ignition, which may
561 occur if the turbidity current develops from the hydrodynamic instability of a dilute turbid

562 cloud, indirectly resulting from slope failures and/or ground shaking (Parker, 1982;
563 Mulder and Cochonnat, 1996; Piper and Normark, 2009; Hage et al., 2019).

564   The distance travelled by the turbidity current on the basin floor cannot be
565 accurately estimated with a single instrumental record. However the drift plot (Figure
566 6) obtained during the waning phase may be roughly indicative of the distance over
567 which particles have been transported beyond the instrument by the turbidity current.
568 The drift distance is 3.5 km, and, when plotted over the bathymetric map, the drift
569 appears to stay within the depositional fan at the outlet of the cayon, the extension of
570 which is known from sediment sounder profiles (Figure 1). These calculations are only
571 a rough estimate of the distance travelled by suspended particles as only the velocity
572 at 1.5 m above the seafloor is known, and at a single point. Nevertheless, considering
573 that the current strength will decrease with distance on the flat seafloor of the basin, it
574 appears unlikely that sediments spread all over the 15x20 km basin floor as this would
575 require velocities of the order of 1m/s, sustained over a wide area for several hours.

576   The decay of the backscatter signal strength over the next three days may
577 reflect the settling of sand size particles, likely clay aggregates, from a dilute
578 suspension. This decay occurs in large part after the 9 hour waning phase of the
579 turbidity current, while current velocity remains lower than 4 cm/s. For a first order
580 assessment, Stokes settling velocity, an upper bound valid in dilute suspensions (e.g.
581 Guazelli and Morris, 2012) may be used. The Stokes settling velocity of 63 µm quartz
582 grains (density 2650 kg/m^3) in 13°C seawater is 2.7 mm/s, allowing such grains to drop
583 by 700 m in three days. However, if the particles forming the cloud are mostly
584 composed of clay agregates, which density may be between 1200 and 1700 kg/m^3,
585 the settling velocity would be comprised between 0.3 mm and 1 mm/s. In this case the
586 height of the suspended particle cloud could range between 70 and 250 m.

587

588   4.2. Current observations across the earthquake magnitude range

589   In this study a seafloor device located at the oultet of a canyon in the Central
590 Basin in the Sea of Marmara recorded a range of turbid events and currents induced
591 by earthquakes that has been rarely documented. In September 2019, M_w 4.7 and 5.8
592 earthquakes occurred at a 5 km distance from the device as well as a series of smaller
593 foreshocks and aftershocks. In this setting, earthquakes of magnitudes less than 4 did
594 not cause noticeable water column turbidity nor currents. The M_w 4.7 earthquake

595 generated a turbid cloud on slopes a few hundred meters from the instrument and the

596 cloud took 3-4 hours to drift down to the instrument location and 10 more hours to

597 dissipate. As the current velocity remained small (less than 4 cm/s), it can be concluded

598 that this cloud did not evolve into a self-sustained turbidity current (Parker, 1982). The

599 M_w 5.8 earthquake initiated a turbidity current and the data obtained may be compared

600 with more complete records obtained elsewhere with ADCP deployments and/or water

601 column mooring lines. A velocity of several tens of centimeter per second is

602 representative of the slower recorded examples, corresponding to mud rich flows

603 associated with hyperpycnal flows or small landslides (Khripounoff et al. 2012), or to

604 the smaller storm-related events (Normandeau et al., 2019). The event recorded is a

605 very weak event compared to turbidity currents that followed large earthquakes or large

606 slope instabilities. Cable breaks shows that the turbidity current triggered by the Grand

607 Banks 1929 earthquake, M_s 7.2, reached velocities of at least 19 m/s (Piper et al.,

608 1999). Velocity of turbidity currents estimated form cable breaks in the Gaoping

609 Canyon and Manilla Trench system range 5.5-12.7 m/s for the M_L 7.0 Pingtung

610 earthquake in 2006 and 5.9-7.9 m/s for a M_L 6.4 earthquake (Gavey et al., 2017). From

611 instrumental records, velocities of 2-7 m/s were reported for the turbidity current

612 following Tohoku M_w 9.1 earthquake (Arai et al., 2013) and 1.4 m/s in the Tokachi-Oki

613 M_w 8.3 case (Mikada et al., 2006). The downward current after the off-Izu Penninsula

614 earthquake may be constrained with a noisy ADCP record to a maximum of 10-15 cm/s

615 in a 20-30 m layer above the seafloor and lasted about one hour, peaking about 30

616 minutes after the earthquake (Kasaya et al., 2009). This turbidity current thus appears

617 less intense and shorter in duration than the one recorded in the Sea of Marmara, but

618 the triggering earthquake was probably smaller (M 5.4 compared to M_W 5.8) and more

619 distant (10 km). Moreover, the off-Izu event shares an important characteristic with the

620 Sea of Marmara one in that the turbid cloud is observed to form some time before

621 current builds up in the water column. When the maximum velocities reported are

622 plotted against magnitude (Figure 9), they show a tendency for larger earthquakes to

623 trigger stronger currents, which is hardly surprising. It also appears that estimates from

624 cable breaks tend to give higher value than instrumental records. This may perhaps

625 be because instruments give the maximum current speed at a single position while

626 cable breaks yield an integrated estimation of maximum current speed. Moreover, if

627 cable breaks are caused by a dense basal flow, it is yet unclear how its speed relates

628 to that of currents in the water column (Paul et al., 2018). The data set available today

629   remains insufficient to reach general conclusions regarding scaling, and other factors
630   than earthquake magnitude, such as slope, would need to be taken into account.

631
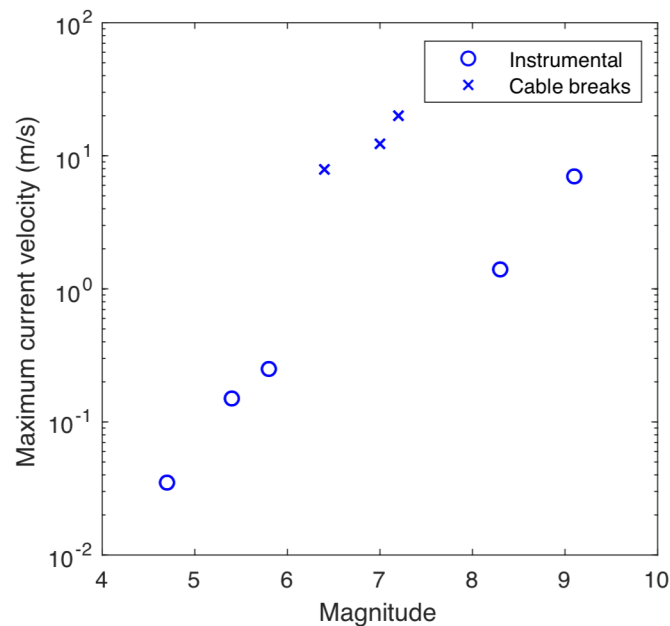
632   **Figure 9.** Maximum measured current velocity as a function of earthquake

633   magnitude for the cases discussed in text.

634

635   4.3.   Implications for sediment transport after earthquakes

636   Several observations from the monitoring records have special relevance for the

637   understanding of sediment resuspension and transport processes during earthquakes.

638   The first one is that earthquakes can induce sediment resuspension in situations where

639   current remains too low to be the primary cause or resuspension. This is apparent went

640   comparing events on Sept 20 (unrelated to earthquake and without turbidity) and Sept

641   24 (after M_w 4.7 earthquake and turbid) that have comparable current speeds.

642   Resuspension may be an immediate effect of ground shaking or results from local

643   slope failures. This process may be important as it opens the possibility of triggering

644   turbidity currents after earthquakes by hydrodynamic instability within the water column.

645   The second one is that a mass flow sufficiently strong and dense to displace a heavy

646   instrument occurred at a time when there was no indication of advection in the water

647   column. Currents in the water column apparently continued to increase in strength after

648   this initial mass flow had stopped. A third observation is that the water displaced with

649   the turbidity currents is deep water, as indicated by the temperature record. Likely, the

650   displaced water originate from where the earthquake triggered sediment mobilization,

651   that is in relatively deep water around the earthquake source area north and west of

652 the instrument location (Figure 1). Turbidity currents more commonly originate from
653 continental shelf edges or the upper part of continental slopes. This is notably the case
654 when they are related to storms, river discharge or sediment loading. However,
655 triggering by earthquakes may affect any part of the continental slope depending on
656 the location of active faults. The case we reported shows that a moderate earthquake
657 (M_w 5.8) can cause sediment remobilization near the base of the slope rather than at
658 the shelf edge resulting in different flow dynamics than generally assumed for sediment
659 remobilization events.

660   The geomorphological context of the deployment site also needs to be taken
661 into account. It is located on a depositional fan at the outlet of a canyon and south of
662 a slope identified as unstable from geomorphological criteria (Zitter et al., 2012). We
663 have shown that a debris flow or dense mud flow originating from this unstable slope,
664 followed several hours later by a turbidity current flowing along the canyon could well
665 explain the sequence of event following the M_w 5.8 earthquake. Although this is not the
666 only possible explanation for the observations, we believe it is the most likely one
667 considering the geomorphological context. We estimated that the current during this
668 event was probably too weak to spread a layer of sediment over the entire Central
669 Basin floor. It is also unclear whether this event left on the fan a sedimentary layer that
670 may be identified as a seismoturbidite, as a debris flow or as a layer of homogeneous
671 mud. Differences between the fan and the basin in the number of sedimentary events
672 and of their characteristics could explain why the sequence of seismic reflectors on
673 sediment sounder profiles differs in the basin and in the fan (Figure 1). For all these
674 reasons, the base of slope or canyon outlets are not good sampling locations for
675 obtaining reliable earthquake records. In previous studies in the Sea of Marmara (e.g.
676 McHugh et al., 2014), samples were taken across the basin depocenter for this
677 purpose and events correlated between cores could also be correlated with historical
678 earthquakes of estimated magnitude > 6.8. This approach remains in principle valid.

5. Conclusion

680   Instrumental records obtained in the Sea of Marmara Central Basin near the
681 base of an unstable slope and the outlet of a canyon bring some insight on sediment
682 remobilization by proximal (≈5 km) earthquakes and their hydrodynamic
683 consequences.

684   -The smaller earthquakes (Mw < 4) are not associated with water column events

685   -A M_w = 4.7 earthquake caused the formation of a turbid cloud and low currents

686   not exceeding 4 cm/s.

687   - A M_w = 5.8 earthquake at the same location caused a mass flow strong enough

688   to capsize a heavy instrument. Subsequent movements of the water masses remained

689   local, mixing deep waters at a scale of 5-to-10 km maximum.

690   This suggests that a continuum of hydrodynamic events of increasing intensity

691   with earthquake magnitude occur above a threshold, corresponding to $Mw \approx 4$ at the

692   studied location. Moderate earthquakes can thus generate mass flows and turbidity

693   currents of limited extension that may confuse paleoseismological records in cores

694   taken near the edges of basins. However, the local nature of these events may help

695   distinguish them from the consequences of storms and floods, expected to initiate from

696   near the edge of the continental shelf. Performing new core studies and very high-

697   resolution geophysical surveys in this area would thus have important implications for

698   understanding under which conditions earthquakes leave a distinctive trace in the

699   sediment record.

700

701   Acknowledgements

702   Financial support was provided by the bilateral ANR/TÜBITAK collaborative research

703   project MAREGAMI (ANR-16-CE03-0010-02 and Tübitak Project 116Y371) and by

704   CNRS-INSU through the European Multidisciplinary Sea Observatory (EMSO)

705   Research Infrastructure program. DT-INSU and Istanbul Technical University

706   hydrodynamic engineering department provided technical support for device design,

707   construction, and deployment. Bernard Mercier de Lépinay provided processed

708   sediment sounder profiles. We thank the crew and Captain of R/V Yunus (Istanbul

709   University) for their support during installation and recovery of the instruments.

710   Seafloor monitoring data are available through SEANOE (Henry et al., 2021) and

711   CTD profile data through SISMER Oceanographic Data portal (Henry et al., 2007).

712

References

714   Adams, J. (1990). Paleoseismicity of the Cascadia Subduction Zone: Evidence from turbidites off the

715   Oregon-Washington Margin. *Tectonics*, *9*(4), 569–583.

716   https://doi.org/10.1029/TC009i004p00569

717 Alpar, B., & Yüce, H. (1998). Sea-level variations and their interactions between the Black
718   Sea nd the Aegean Sea. Estuarine, Coastal and Shelf Science, 46, 609–619.

719 Arai, K., Naruse, H., Miura, R., Kawamura, K., Hino, R., Ito, Y., Inazu, D., Yokokawa, M.,
720   Izumi, N., Murayama, M., & Kasaya, T. (2013). Tsunami-generated turbidity current of
721   the 2011 Tohoku-Oki earthquake. Geology, 41(11), 1195–1198.
722   https://doi.org/10.1130/G34777.1

723 Atwater, B. F., Carson, B., Griggs, G. B., Johnson, P. P., & Salmi, M. S. (2014). Rethinking
724   turbidite paleoseismology along the Cascadia subduction zone. *Geology*, *42*(9), 827–
725   830. https://doi.org/10.1130/G35902.1

726 Armijo, R., Meyer, B., Navarro, S., King, G., & Barka, A. (2002). Asymmetric slip partitioning
727   in the Sea of Marmara pull-apart: a clue to propagation processes of the North Anatolian
728   Fault? Terra Nova, 14(2), 80–86. https://doi.org/10.1046/j.1365-3121.2002.00397.x

729 Armijo, R. and J. Malavieille (2002) MARMARASCARPS cruise, RV L'Atalante,
730   https://doi.org/10.17600/2010140

731 Azpiroz-Zabala, M., Cartigny, M. J. B., Talling, P. J., Parsons, D. R., Sumner, E. J., Clare, M.
732   A., Simmons, S. M., Cooper, C., & Pope, E. L. (2017). Newly recognized turbidity current
733   structure can explain prolonged flushing of submarine canyons. Science Advances,
734   3(10). https://doi.org/10.1126/sciadv.1700200

735 Beck, C., Mercier de Lépinay, B., Schneider, J. L., Cremer, M., Çağatay, N., Wendenbaum,
736   E., et al. (2007). Late Quaternary co-seismic sedimentation in the Sea of Marmara's
737   deep basins. Sedimentary Geology, 199, 65–89.
738   https://doi.org/10.1016/j.sedgeo.2005.12.031

739 Beşiktepe, Ş. T., Sur, H. İ., Özsoy, E., Latif, M. A., Oğuz, T., & Ünlüata, Ü. (1994). The
740   circulation and hydrography of the Marmara Sea. Progress in Oceanography, 34(4),
741   285–334. https://doi.org/10.1016/0079-6611(94)90018-3

742 Bradley, B. A., Razafindrakoto, H. N. T., & Polak, V. (2017). Ground-Motion Observations
743   from the 14 November 2016 M w 7.8 Kaikoura, New Zealand, Earthquake and Insights
744   from Broadband Simulations. *Seismological Research Letters*, *88*(3), 740–756.
745   https://doi.org/10.1785/0220160225

746 Brizuela, N., Filonov, A., & Alford, M. H. (2019). Internal tsunami waves transport sediment
747   released by underwater landslides. Scientific Reports, 9(1), 10775.
748   https://doi.org/10.1038/s41598-019-47080-0

749 Bulut, F., Aktuğ, B., Yaltırak, C., Doğru, A., & Özener, H. (2019). Magnitudes of future large
750   earthquakes near Istanbul quantified from 1500 years of historical earthquakes, present-
751   day microseismicity and GPS slip rates. Tectonophysics, 764(July 2018), 77–87.
752   https://doi.org/10.1016/j.tecto.2019.05.005

753 Çağatay, M. N., Erel, L., Bellucci, L. G., Polonia, a., Gasperini, L., Eriş, K. K., Sancar, Ü.,
754   Biltekin, D., Uçarkuş, G., Ülgen, U. B., & Damci, E. (2012). Sedimentary earthquake
755   records in the İzmit Gulf, Sea of Marmara, Turkey. Sedimentary Geology, 282, 347–359.
756   https://doi.org/10.1016/j.sedgeo.2012.10.001

757 Çağatay, N. M., Ucarkus, G., Eris, K. K., Henry, P., Gasperini, L., & Polonia, A. (2015).
758   Submarine canyons of the Sea of Marmara. In F. Briand (Ed.), Submarine Canyon
759   Dynamics in the Mediterranean and Tributary Seas, CIESM Workshop Monograph n° 47
760   (pp. 123–135). CIESM Publisher, Monaco. https://doi.org/10.13140/RG.2.1.1692.8402

761 Carter, L., Milliman, J. D., Talling, P. J., Gavey, R., & Wynn, R. B. (2012). Near-synchronous
762   and delayed initiation of long run-out submarine sediment flows from a record-breaking
763   river flood, offshore Taiwan. *Geophysical Research Letters*, *39*(12), 6–10.
764   https://doi.org/10.1029/2012GL051172

765 Cattaneo, A., Babonneau, N., Ratzov, G., Dan-Unterseh, G., Yelles, K., Bracane, R., Mercier
766   De Lapinay, B., Boudiaf, A., & Daverchare, J. (2012). Searching for the seafloor
767   signature of the 21 May 2003 Boumerdas earthquake offshore central Algeria. Natural
768   Hazards and Earth System Science, 12(7), 2159–2172. https://doi.org/10.5194/nhess-
769   12-2159-2012

770 Dan, G., Sultan, N., Savoye, B., Deverchere, J., & Yelles, K. (2009). Quantifying the role of
771   sandy-silty sediments in generating slope failures during earthquakes: Example from the
772   Algerian margin. International Journal of Earth Sciences, 98(4), 769–789.
773   https://doi.org/10.1007/s00531-008-0373-5

774 Drab, L., Hubert Ferrari, A., Schmidt, S., & Martinez, P. (2012). The earthquake sedimentary
775   record in the western part of the Sea of Marmara, Turkey. Natural Hazards and Earth
776   System Science, 12(4), 1235–1254. https://doi.org/10.5194/nhess-12-1235-2012

777 Drab, L., Hubert-Ferrari, A., Schmidt, S., Martinez, P., Carlut, J., & El Ouahabi, M. (2015).
778   Submarine Earthquake History of the Çınarcık Segment of the North Anatolian Fault in
779   the Marmara Sea, Turkey. Bulletin of the Seismological Society of America, 105(2A),
780   622–645. https://doi.org/10.1785/0120130083

781 Eriş, K. K., Çağatay, N., Beck, C., Mercier de Lepinay, B., & Corina, C. (2012). Late-
782   Pleistocene to Holocene sedimentary fills of the Çinarcik Basin of the Sea of Marmara.
783   Sedimentary Geology, 281, 151–165. https://doi.org/10.1016/j.sedgeo.2012.09.001

784 Garfield, N., Rago, T. A., Schnebele, K. J., & Collins, C. A. (1994). Evidence of a turbidity
785   current in Monterey Submarine Canyon associated with the 1989 Loma Prieta
786   earthquake. Continental Shelf Research, 14(6), 673–686. https://doi.org/10.1016/0278-
787   4343(94)90112-0

788 Gavey, R., Carter, L., Liu, J. T., Talling, P. J., Hsu, R., Pope, E., & Evans, G. (2017).
789   Frequent sediment density flows during 2006 to 2015, triggered by competing seismic

790   and weather events: Observations from subsea cable breaks off southern Taiwan.

791   *Marine Geology*, *384*, 147–158. https://doi.org/10.1016/j.margeo.2016.06.001

792   Goldfinger, C., Nelson, C. H., & Johnson, J. E. (2003). Holocene earthquake records from

793   the cascadia subduction zone and northern san andreas fault based on precise dating of

794   offshore turbidites. Annual Review of Earth and Planetary Sciences, 31(1), 555–577.

795   https://doi.org/10.1146/annurev.earth.31.100901.141246

796   Goldfinger, C., Nelson, C. H., Morey, A. E., Johnson, J. E., Patton, J., Karabanov, E.,

797   Gutiérrez-Pastor, J., Eriksson, A. T., Gràcia, E., Dunhill, G., Enkin, R. J., Dallimore, A., &

798   Vallier, T. (2012). Earthquake Hazards of the Pacific Northwest Coastal and Marine

799   Regions Turbidite Event History — Methods and Implications for Holocene

800   Paleoseismicity of the Cascadia Subduction Zone Professional Paper 1661 – F. USGS,

801   Professional Paper 1661-F, 170. Retrieved from http://pubs.usgs.gov/pppp1661f/

802   Grall, C., Henry, P., Tezcan, D., Mercier de Lepinay, B., Becel, A., Geli, L., Rudkiewicz, J.-L.,

803   Zitter, T., & Harmegnies, F. (2012). Heat flow in the Sea of Marmara Central Basin:

804   Possible implications for the tectonic evolution of the North Anatolian fault. Geology,

805   40(1), 3–6. https://doi.org/10.1130/G32192.1

806   Guazzelli, E., Morris, J. F., & Pic, S. (2011). A Physical Introduction to Suspension

807   Dynamics. Cambridge: Cambridge University Press.

808   https://doi.org/10.1017/CBO9780511894671

809   Guerrero, M., Rüther, N., & Szupiany, R. N. (2012). Laboratory validation of acoustic Doppler

810   current profiler (ADCP) techniques for suspended sediment investigations. Flow

811   Measurement and Instrumentation, 23(1), 40–48.

812   https://doi.org/10.1016/j.flowmeasinst.2011.10.003

813   Guerrero, M., Szupiany, R. N., & Amsler, M. (2011). Comparison of acoustic backscattering

814   techniques for suspended sediments investigation. Flow Measurement and

815   Instrumentation, 22(5), 392–401. https://doi.org/10.1016/j.flowmeasinst.2011.06.003

816   Gutiérrez-Pastor, J., Nelson, C. H., Goldfinger, C., & Escutia, C. (2013). Sedimentology of

817   seismo-turbidites off the Cascadia and northern California active tectonic continental

818   margins, northwest Pacific Ocean. Marine Geology, 336, 99–119.

819   https://doi.org/10.1016/j.margeo.2012.11.010

820   Gwyn Lintern, D., Hill, P. R., & Stacey, C. (2016). Powerful unconfined turbidity current

821   captured by cabled observatory on the fraser river delta slope, British Columbia, Canada.

822   *Sedimentology*, *63*(5), 1041–1064. https://doi.org/10.1111/sed.12262

823   Hage, S., Cartigny, M. J. B., Sumner, E. J., Clare, M. A., Hughes Clarke, J. E., Talling, P. J.,

824   et al. (2019). Direct Monitoring Reveals Initiation of Turbidity Currents From Extremely

825   Dilute River Plumes. *Geophysical Research Letters*, *46*(20), 11310–11320.

826   https://doi.org/10.1029/2019GL084526

827 Hébert, H., Schindelé, F., Altinok, Y., Alpar, B., & Gazioglu, C. (2005). Tsunami hazard in the
828   Marmara Sea (Turkey): A numerical approach to discuss active faulting and impact on
829   the Istanbul coastal areas. Marine Geology, 215, 23–43.
830   https://doi.org/10.1016/j.margeo.2004.11.006

831 Heezen, B. C., Ericson, D. B., & Ewing, M. (1954). Further evidence for a turbidity current
832   following the 1929 Grand banks earthquake. Deep Sea Research (1953), 1(4), 193–202.
833   https://doi.org/10.1016/0146-6313(54)90001-5

834 Heerema, C. J., Cartigny, M. J. B., Jacinto, R. S., Simmons, S. M., Apprioual, R., & Talling,
835   P. J. (2022). How distinctive are flood-triggered turbidity currents? *Journal of*
836   *Sedimentary Research*, *92*(1), 1–11. https://doi.org/10.2110/jsr.2020.168

837 Henry, P., A.M.C. Şengör, M.N. Çağatay (2007) MARNAUT cruise, RV L'Atalante,
838   https://doi.org/10.17600/7010070

839 Henry, P., Özeren M.S., Desprez De Gesincourt O., de Saint-Leger E., Libes,, M., Çakir, Z.,
840   Yakupoğlu, N., Géli, L. (2021). EMSO / MAREGAMI Marmara bottom pressure and
841   current records. SEANOE. https://doi.org/10.17882/78928

842 Hersbach, H., Bell, B., Berrisford, P., Biavati, G., Horányi, A., Muñoz Sabater, J., Nicolas, J.,
843   Peubey, C., Radu, R., Rozum, I., Schepers, D., Simmons, A., Soci, C., Dee, D., Thépaut,
844   J-N. (2018): ERA5 hourly data on single levels from 1959 to present. Copernicus Climate
845   Change Service (C3S) Climate Data Store (CDS).
846   https://doi.org/10.24381/cds.adbb2d47

847 Howarth, J. D., Orpin, A. R., Kaneko, Y., Strachan, L. J., Nodder, S. D., Mountjoy, J. J.,
848   Barnes, P. M., Bostock, H. C., Holden, C., Jones, K., & Cağatay, M. N. (2021).
849   Calibrating the marine turbidite palaeoseismometer using the 2016 Kaikōura earthquake.
850   *Nature Geoscience*, *14*(3), 161–167. https://doi.org/10.1038/s41561-021-00692-6

851 Hsu, S. K., Kuo, J., Lo, C. L., Tsai, C. H., Doo, W. Bin, Ku, C. Y., & Sibuet, J. C. (2008).
852   Turbidity currents, submarine landslides and the 2006 Pingtung earthquake off SW
853   Taiwan. Terrestrial, Atmospheric and Oceanic Sciences, 19(6), 767–772.
854   https://doi.org/10.3319/TAO.2008.19.6.767(PT)

855 Hughes Clarke, J. E. (2016). First wide-angle view of channelized turbidity currents links
856   migrating cyclic steps to flow characteristics. Nature Communications, 7(1), 11896.
857   https://doi.org/10.1038/ncomms11896

858 Ikehara, K., Kanamatsu, T., Nagahashi, Y., Strasser, M., Fink, H., Usami, K., et al. (2016).
859   Documenting large earthquakes similar to the 2011 Tohoku-oki earthquake from
860   sediments deposited in the Japan Trench over the past 1500 years. Earth and Planetary
861   Science Letters, 445, 48–56. doi:10.1016/j.epsl.2016.04.009

862 Johnson, H. P., Gomberg, J. S., Hautala, S. L., & Salmi, M. S. (2017). Sediment gravity flows

863   triggered by remotely generated earthquake waves. *Journal of Geophysical Research:*

864   *Solid Earth*, *122*(6), 4584–4600. https://doi.org/10.1002/2016JB013689

865 Karabulut, H., Güvercin, S. E., Eskikoÿ, F., Konca, A. Ö., & Ergintav, S. (2021). The

866   moderate size 2019 September Mw5.8 Silivri earthquake unveils the complexity of the

867   Main Marmara Fault shear zone. Geophysical Journal International, 224(1), 377–388.

868   https://doi.org/10.1093/gji/ggaa469

869 Kasaya, T., Mitsuzawa, K., Goto, T., Iwase, R., Sayanagi, K., Araki, E., Asakawa, K., Mikada,

870   H., Watanabe, T., Takahashi, I., & Nagao, T. (2009). Trial of Multidisciplinary

871   Observation at an Expandable Sub-Marine Cabled Station "Off-Hatsushima Island

872   Observatory" in Sagami Bay, Japan. Sensors, 9(11), 9241–9254.

873   https://doi.org/10.3390/s91109241

874 Khripounoff, A., Crassous, P., Lo Bue, N., Dennielou, B., & Silva Jacinto, R. (2012). Different

875   types of sediment gravity flows detected in the Var submarine canyon (northwestern

876   Mediterranean Sea). Progress in Oceanography, 106, 138–153.

877   https://doi.org/10.1016/j.pocean.2012.09.001

878 Le Pichon, X., Chamot-Roooke, N., Rangin, C., & Sengör, A. M. C. (2003). The North

879   Anatolian fault in the Sea of Marmara. Journal of Geophysical Research, 108, 2179.

880   https://doi.org/10.1029/2002JB001862

881 Le Pichon, X., Şengör, A. M. C., Demirbağ, E., Rangin, C., İmren, C., Armijo, R., Görür, N.,

882   Çağatay, N., Mercier de Lepinay, B., Meyer, B., Saatçılar, R., & Tok, B. (2001). The

883   active Main Marmara Fault. Earth and Planetary Science Letters, 192(4), 595–616.

884   https://doi.org/10.1016/S0012-821X(01)00449-6

885 Liu, J. T., Wang, Y.-H., Yang, R. J., Hsu, R. T., Kao, S.-J., Lin, H.-L., & Kuo, F. H. (2012).

886   Cyclone-induced hyperpycnal turbidity currents in a submarine canyon. Journal of

887   Geophysical Research: Oceans, 117(C4), n/a-n/a.

888   https://doi.org/10.1029/2011JC007630

889 McDougall, T. J., & Barker, P. M. (2011). Getting started with TEOS-10 and the Gibbs

890   Seawater (GSW) oceanographic toolbox. Scor/Iapso WG, 127, 1-28.

891 McDougall, T. J., Feistel, R., & Pawlowicz, R. (2013). Thermodynamics of Seawater. In

892   International Geophysics (2nd ed., Vol. 103, pp. 141–158). Elsevier Ltd.

893   https://doi.org/10.1016/B978-0-12-391851-2.00006-4

894 McHugh, C. M. G., Seeber, L., Cormier, M. H., Dutton, J., Cagatay, N., Polonia, A., Ryan, W.

895   B. F., & Gorur, N. (2006). Submarine earthquake geology along the North Anatolia Fault

896   in the Marmara Sea, Turkey: A model for transform basin sedimentation. Earth and

897   Planetary Science Letters, 248, 661–684. https://doi.org/10.1016/j.epsl.2006.05.038

898 McHugh, C. M., Seeber, L., Braudy, N., Cormier, M. H., Davis, M. B., Diebold, J. B.,
899   Dieudonne, N., Douilly, R., Gulick, S. P. S., Hornbach, M. J., Johnson, H. E., Mishkin, K.
900   R., Sorlien, C. C., Steckler, M. S., Symithe, S. J., & Templeton, J. (2011). Offshore
901   sedimentary effects of the 12 January 2010 Haiti earthquake. Geology, 39(8), 723–726.
902   https://doi.org/10.1130/G31815.1

903 McHugh, C. M. G., Braudy, N., Çağatay, M. N., Sorlien, C., Cormier, M.-H., Seeber, L., &
904   Henry, P. (2014). Seafloor fault ruptures along the North Anatolia Fault in the Marmara
905   Sea, Turkey: Link with the adjacent basin turbidite record. Marine Geology, 353, 65–83.
906   https://doi.org/10.1016/j.margeo.2014.03.005

907 Mikada, H., Mitsuzawa, K., Matsumoto, H., Watanabe, T., Morita, S., Otsuka, R., Sugioka,
908   H., Baba, T., Araki, E., & Suyehiro, K. (2006). New discoveries in dynamics of an M8
909   earthquake-phenomena and their implications from the 2003 Tokachi-oki earthquake
910   using a long term monitoring cabled observatory. Tectonophysics, 426(1–2), 95–105.
911   https://doi.org/10.1016/j.tecto.2006.02.021

912 Mountjoy, J. J., Howarth, J. D., Orpin, A. R., Barnes, P. M., Bowden, D. A., Rowden, A. A.,
913   Schimel, A. C. G., Holden, C., Horgan, H. J., Nodder, S. D., Patton, J. R., Lamarche, G.,
914   Gerstenberger, M., Micallef, A., Pallentin, A., & Kane, T. (2018). Earthquakes drive large-
915   scale submarine canyon development and sediment supply to deep-ocean basins.
916   Science Advances, 4(3), 1–9. https://doi.org/10.1126/sciadv.aar3748

917 Mulder, T., & Cochonnat, P. (1996). Classification of Offshore Mass Movements. SEPM
918   Journal of Sedimentary Research, Vol. 66. https://doi.org/10.1306/D42682AC-2B26-
919   11D7-8648000102C1865D

920 Mulder, T., Syvitski, J. P. M., Migeon, S., Faugères, J.-C., & Savoye, B. (2003). Marine
921   hyperpycnal flows: initiation, behavior and related deposits. A review. Marine and
922   Petroleum Geology, 20(6–8), 861–882. https://doi.org/10.1016/j.marpetgeo.2003.01.003

923 Nakajima, T., & Kanai, Y. (2000). Sedimentary features of seismoturbidites triggered by the
924   1983 and older historical earthquakes in the eastern margin of the Japan Sea.
925   Sedimentary Geology, 135(1–4), 1–19. https://doi.org/10.1016/S0037-0738(00)00059-2

926 Normandeau, A., Bourgault, D., Neumeier, U., Lajeunesse, P., St-Onge, G., Gostiaux, L., &
927   Chavanne, C. (2020). Storm-induced turbidity currents on a sediment-starved shelf:
928   Insight from direct monitoring and repeat seabed mapping of upslope migrating
929   bedforms. Sedimentology, 67(2), 1045–1068. https://doi.org/10.1111/sed.12673

930 Okal, E. A., & Synolakis, C. E. (2001). Comment on "Origin of the 17 July 1998 Papua New
931   Guinea Tsunami: Earthquake or Landslide?" by E. L. Geist. Seismological Research
932   Letters, 72(3), 362–366. https://doi.org/10.1785/gssrl.72.3.362

933 Özeren, M. S., Çağatay, M. N., Postacioğlu, N., Şengör, a. M. C., Görür, N., & Eriş, K.
934   (2010). Mathematical modelling of a potential tsunami associated with a late glacial

935   submarine landslide in the Sea of Marmara. Geo-Marine Letters, 30, 523–539.

936   https://doi.org/10.1007/s00367-010-0191-1

937   Palanques, A., Guillén, J., Puig, P., & Durrieu de Madron, X. (2008). Storm-driven shelf-to-

938   canyon suspended sediment transport at the southwestern Gulf of Lions. *Continental*

939   *Shelf Research*, *28*(15), 1947–1956. https://doi.org/10.1016/j.csr.2008.03.020

940   Parker, G. (1982). Conditions for the ignition of catastrophically erosive turbidity currents.

941   Marine Geology, 46(3–4), 307–327. https://doi.org/10.1016/0025-3227(82)90086-X

942   Paull, C. K., Talling, P. J., Maier, K. L., Parsons, D., Xu, J., Caress, D. W., et al. (2018).

943   Powerful turbidity currents driven by dense basal layers. *Nature Communications*, *9*(1),

944   1–9. https://doi.org/10.1038/s41467-018-06254-6

945   Piper, D. J. W., & Normark, W. R. (2009). Processes That Initiate Turbidity Currents and

946   Their Influence on Turbidites: A Marine Geology Perspective. Journal of Sedimentary

947   Research, 79(6), 347–362. https://doi.org/10.2110/jsr.2009.046

948   Piper, D. J. W., Cochonat, P., & Morrison, M. L. (1999). The sequence of events around the

949   epicentre of the 1929 Grand Banks earthquake: initiation of debris flows and turbidity

950   current inferred from sidescan sonar. Sedimentology, 46(1), 79–97.

951   https://doi.org/10.1046/j.1365-3091.1999.00204.x

952   Polonia, A., Vaiani, S. C., & De Lange, G. J. (2016). Did the A.D. 365 Crete

953   earthquake/tsunami trigger synchronous giant turbidity currents in the Mediterranean

954   Sea? Geology, 44(3), 191–194. https://doi.org/10.1130/G37486.1

955   Polonia, A., Nelson, C. H., Romano, S., Vaiani, S. C., Colizza, E., Gasparotto, G., &

956   Gasperini, L. (2017). A depositional model for seismo-turbidites in confined basins based

957   on Ionian Sea deposits. *Marine Geology*, *384*, 177–198.

958   https://doi.org/10.1016/j.margeo.2016.05.010

959   Pope, E. L., Talling, P. J., & Carter, L. (2017). Which earthquakes trigger damaging

960   submarine mass movements: Insights from a global record of submarine cable breaks?

961   Marine Geology, 384, 131–146. https://doi.org/10.1016/j.margeo.2016.01.009

962   Puig, P., Ogston, A. S., Mullenbach, B. L., Nittrouer, C. A., Parsons, J. D., & Sternberg, R.

963   W. (2004). Storm-induced sediment gravity flows at the head of the Eel submarine

964   canyon, northern California margin. *Journal of Geophysical Research: Oceans*, *109*(C3),

965   1–10. https://doi.org/10.1029/2003JC001918

966   Şengör, A. M. C., Grall, C., İmren, C., Le Pichon, X., Görür, N., Henry, P., Karabulut, H., &

967   Siyako, M. (2014). The geometry of the North Anatolian transform fault in the Sea of

968   Marmara and its temporal evolution: implications for the development of intracontinental

969   transform faults. Canadian Journal of Earth Sciences, 51(3), 222–242.

970   https://doi.org/10.1139/cjes-2013-0160

971   Synolakis, C. E., Bardet, J.-P., Borrero, J. C., Davies, H. L., Okal, E. A., Silver, E. A., Sweet,

972   S., & Tappin, D. R. (2002). The slump origin of the 1998 Papua New Guinea Tsunami.

973   Proceedings of the Royal Society of London. Series A: Mathematical, Physical and

974   Engineering Sciences, 458(2020), 763–789. https://doi.org/10.1098/rspa.2001.0915

975   Talling, P. J. (2021). Fidelity of turbidites as earthquake records. *Nature Geoscience, 14*(3),

976   113–116. https://doi.org/10.1038/s41561-021-00707-2

977   Talling, P. J., Masson, D. G., Sumner, E. J., & Malgesini, G. (2012). Subaqueous sediment

978   density flows: Depositional processes and deposit types. *Sedimentology*, *59*(7), 1937–

979   2003. https://doi.org/10.1111/j.1365-3091.2012.01353.x

980   Xu, J. P., Noble, M. A., & Rosenfeld, L. K. (2004). In-situ measurements of velocity structure

981   within turbidity currents. Geophysical Research Letters, 31(9).

982   https://doi.org/10.1029/2004GL019718

983   Xu, J. P., Swarzenski, P. W., Noble, M., & Li, A.-C. (2010). Event-driven sediment flux in

984   Hueneme and Mugu submarine canyons, southern California. Marine Geology, 269(1–

985   2), 74–88. https://doi.org/10.1016/j.margeo.2009.12.007

986   Yakupoğlu, N., Uçarkuş, G., Kadir Eriş, K., Henry, P., & Namık Çağatay, M. (2019).

987   Sedimentological and geochemical evidence for seismoturbidite generation in the

988   Kumburgaz Basin, Sea of Marmara: Implications for earthquake recurrence along the

989   Central High Segment of the North Anatolian Fault. Sedimentary Geology, 380, 31–44.

990   https://doi.org/10.1016/j.sedgeo.2018.11.002

991   Zitter, T. A. C., Grall, C., Henry, P., Özeren, M. S., Çağatay, M. N., Şengör, A. M. C.,

992   Gasperini, L., de Lépinay, B. M., & Géli, L. (2012). Distribution, morphology and triggers

993   of submarine mass wasting in the Sea of Marmara. Marine Geology, 329–331, 58–74.

994   https://doi.org/10.1016/j.margeo.2012.09.002